Impact of Structural Defects on the Photocatalytic Properties of Zno

Nouha Mediouni, Chantal Guillard, Frederic Dappozze, Lhoussain Khrouz, Stephane Parola, Christophe Colbeau-Justin, Abdesslem Ben Haj Amara, Hafsia Ben Rhaiem, Nicole Jaffrezic-Renault, Philippe Namour

Impact of structural defects on the photocatalytic properties of ZnO

Nouha Mediouni , Chantal Guillard , Frederic Dappozze , Lhoussain Khrouz , Stephane Parola , Christophe Colbeau-Justin , Abdesslem Ben Haj Amara , Hafsia Ben Rhaiem , Nicole Jaffrezic-Renault , Philippe Namour

PII: S2772-4166(22)00037-7
DOI: https://doi.org/10.1016/j.hazadv.2022.100081
Reference: HAZADV 100081

To appear in: *Journal of Hazardous Materials Advances*

Received date: 17 February 2022
Revised date: 8 April 2022
Accepted date: 29 April 2022

Please cite this article as: Nouha Mediouni , Chantal Guillard , Frederic Dappozze , Lhoussain Khrouz , Stephane Parola , Christophe Colbeau-Justin , Abdesslem Ben Haj Amara , Hafsia Ben Rhaiem , Nicole Jaffrezic-Renault , Philippe Namour , Impact of structural defects on the photocatalytic properties of ZnO, *Journal of Hazardous Materials Advances* (2022), doi: https://doi.org/10.1016/j.hazadv.2022.100081

Impact of structural defects on the photocatalytic properties of ZnO

Nouha Mediouni [a,b], Chantal Guillard* [a], Frederic Dappozze [a], Lhoussain Khrouz [d], Stephane Parola [d], Christophe Colbeau-Justin [e], Abdesslem Ben Haj Amara [b], Hafsia Ben Rhaiem [b], Nicole Jaffrezic-Renault[f], Philippe Namour [c]

(a) *Université Lyon 1, Institut De Recherche Sur La Catalyse Et l'Environnement De Lyon (IRCELYON), CNRS, 2 Avenue Albert Einstein, 69626, Villeurbanne, France.*
(b) *Université de Carthage, Faculté des Sciences de Bizerte, Laboratoire Ressource Matériaux et Ecosystème, 7021 Zarzouna, Tunisie.*
(c) *INRAE, UR RiverLy, Centre de Lyon-Grenoble Auvergne-Rhône-Alpes, 5, rue de la Doua CS 20244, F69625 Villeurbanne, France.*
(d) *Université Lyon 1, Ecole Normale Supérieure de Lyon, CNRS, UMR 5182, Laboratoire de Chimie, 46 allée d'Italie, F69364, Lyon, France.*
(e) *Université Paris-Saclay, Institut de Chimie Physique, UMR 8000 CNRS, 91405 Orsay, France.*
(f) *Institute of Analytical Sciences, University of Lyon, 5 rue de la Doua, 69100, Villeurbanne, France*

*Corresponding author: chantal.guillard@ircelyon.univ-lyon1.fr

Highlights

- The use of organic precursor (Zinc Acetate) can release pollutant in water.
- Impact of calcination temperature on structural and photocatalytic properties of ZnO
- Raman and EPR techniques used to determine the structural defects on ZnO semiconductors
- Impact of surface area and surface defects on photocatalysis must be separately considered
- Oxygen and/or zinc vacancies are harmful for photocatalytic properties

Abstract

ZnO photocatalytic materials have been prepared using three precursors (Zinc Acetate, Zinc Hydroxide, and Zinc Peroxide), and the effect of calcination temperature on structural and photocatalytic properties of ZnO has been investigated. XRD, UV-Vis, BET, XPS, Time-Resolved Microwave Conductivity (TRMC), Raman, and Electron Paramagnetic Resonance (EPR) have been used to correlate the impact of the surface area, the introduction of oxygen and/or zinc vacancies, and the charge carrier dynamics, with their photocatalytic properties. The main objective is to provide a new approach to the impact of structural defects on ZnO semiconductors determined by using Raman and EPR techniques, and by coupling with the important role of the surface area

considered as one of the most relevant characteristics in photocatalysis in terms of performance. The fewer surface defects, the more photoactive the catalyst is. The results are discussed for the model degradation of formic acid and phenol under UV-irradiation.

Keywords:

Zinc Oxide, Photocatalysis, Surface area, Structural Defects, Electron Paramagnetic Resonance (EPR).

1. Introduction

Most studies on the photocatalytic degradation of water pollutants are carried out using a TiO_2 catalyst since it proposes one of the most efficient photocatalytic activity, large scale availability (commercial), and stability. It allows the formation of electron/hole pairs (e-/h+), generating highly Reactive Oxygen Species (ROS); such as OH°, O_2°, and HOO° in presence of an irradiation source [1–3]. At the same time, the research activity has focused on finding alternatives to TiO_2 aimed to attend efficient activity toward aqueous contaminants [4]. Among available semiconductors, ZnO is the most studied oxide after TiO_2 and has been proposed as a promising photocatalyst for water treatment [5]. ZnO propose a wide direct bandgap (3.3 eV) allowing absorption of sunlight at higher wavelengths than TiO_2 [6] and, its photocatalytic properties are sometimes more significant than TiO_2 ones [7–9]. Another major difference between ZnO compared to TiO_2 is the possibility to detect the H_2O_2 formation during the photocatalytic process while it degrades rapidly on TiO_2 because of the formation of the Ti-peroxo complex [10,11]. Generally, studies on ZnO focus on its preparation procedure using various methods and precursors, that strongly affect its properties and influence its photocatalytic activity [12–15]. The impact of some properties such as surface area, structural defects, and other classical parameters such as crystallinity or morphology have been widely studied in the literature [16–34]. Unfortunately, the impact of most parameters is still under debate due to their interdependence. Whereas the crystallinity [16,24], and the absence of impurities [35], are generally found essential to obtain a good photocatalytic activity; the impact of the morphology, the surface area, and the presence of defects such as oxygen or zinc vacancies is still not completely elucidated. In some cases, authors reported that the photocatalytic activity of ZnO increased with the increase of surface area due to a decrease in the recombination of photo-generated electron/hole pairs [25,26]. However, Wolski et al [24] considered that a moderate surface area is the best compromise. On the other hand, some publications [16,19], mentioned that a smaller surface area can be more efficient than an important one, highlighting the importance of other parameters such as morphology [16] and the polar planes exposed in the crystal [19]. Concerning

the impact of the morphology, no particular morphology emerges in the literature. Li et al [16] found that needles aggregates present the highest efficiency, even if these latest have very small surface area. While Thakur et al [17] consider that the nanospheres are more adequate for better photocatalytic activity. On the other hand, Zhang et al [18] mentioned that the nanospheres, are more efficient than rods or a butterfly-like ZnO and correlate their efficiency to the presence of polar exposed facets. The importance of the orientation of the planes is in agreement with different publications [18–23]. However, this phenomenon is also linked to different parameters, morphology [18,20], surface area [20], and oxygen vacancies [23]. Another important parameter that is still always under debate in the literature is the impact of oxygen and zinc vacancies. Nandi et al [27] considered that surface defects are beneficial to improving the photocatalytic activity of ZnO. However, whereas some publications consider that the Zn defects are important to improve the photocatalytic activity of ZnO [24,29,30,36], the study of Danilenko et al [31] reported that zinc vacancies are harmful to photocatalysis. They show that oxygen vacancies enhance the photocatalytic activity of ZnO and promote charge separation, in agreement with several other publications [32,33,37,38]. On the other hand, and contrary to the suggestions mentioned above, several other works [28,34] reported an unfavorable impact of oxygen and zinc defects appearing in ZnO on its photocatalytic activity. Consequently, there are still uncertainties in the literature between various relevant parameters, and more experimentation is needed to overcome these contradictions.

The main objective of this paper is to understand the photocatalytic properties of the ZnO-based material about its structural features while evaluating the charge carrier dynamics and the generation of several kinds of defects to associate the distinct physicochemical parameters, and therefore, discuss the impact on photocatalytic efficiency. For this study, the photocatalysts were prepared by using a precipitation method at low temperature, using three precursors with different reactivity, and calcination at various temperatures to generate materials with different surface areas and structural defects. The photocatalytic performance of photocatalysts will be evaluated in presence of two model molecules: Formic acid (FA), an aliphatic compound, that allows direct mineralization to CO_2 and H_2O without the formation of any intermediate species; and phenol, suitable for investigating more complex aromatic water pollutants.

2. Materials and methods

2.1. Materials

Zinc acetate dihydrate ($Zn(CH_3CO_2)_2$ $2H_2O$, Merck); zinc Nitrate ($Zn(NO_3)_2 4H_2O$, Aldrich), KOH from Merck, and NaOH from Chimie Plus were used in the preparation of ZnO samples as described in paragraph 2.2. Milli-Q water (18 MΩ) and methanol (*Semiconductor Grade,* 99.9% pure) from Alfa were used as solvents for all the syntheses and analyses. Hydrogen peroxide (H_2O_2), at 30% in water from Sigma-Aldrich was used in our experiments. Formic acid (99% pure) and Phenol (99% pure) provided by Across Organics were used as a model of pollutants for photocatalytic tests.

2.2. Catalysts

Three ZnO materials were prepared either from direct precipitation of Zn $(CH_3COO)_2$ or via a thermal conversion approach from $Zn(OH)_2$ or ZnO_2.

2.2.1. Preparation from Zn $(CH_3CO_2)_2$

Zn $(CH_3COO)_2$. 2H2O (0.01 M) was precipitated with KOH (0.04 M) in methanol. The mixture was continuously stirred and maintained under reflux at 60°C until a white gel was formed. After the reaction time was achieved, the resulting precipitate was separated from the solution by centrifugation (4500 rpm, t = 15 min), washed several times with distilled water, and dried at 60°C overnight (sample, ZnA60). The obtained powder was then calcinated for 2h under air flux with a heating rate of 5 °C·min-1 at 400°C, 500°C, and 600°C. The samples were respectively named ZnAxT, with x: the temperature of calcination.

2.2.2. Preparation from Zn $(OH)_2$

For preparing $Zn(OH)_2$, the mixing (100mL/100mL) of the two aqueous solutions of $Zn(NO_3)_2.6H_2O$ (1M) and NaOH (2M) was stirred for 2h at room temperature. Then, the precipitate was centrifuged (4500 rpm, t=15 min), washed several times with distilled water, and dried at 25°C for 24h. The obtained hydroxide was annealed for 2h at 400°C, 500°C, or 600°C under the same conditions mentioned above and the samples were labeled as ZnH4T, ZnH5T, and ZnH6T.

2.2.3. Preparation from ZnO_2

A mixture (50mL/50mL) of an aqueous solution of $Zn(OH)_2$ as prepared above, and H_2O_2 (1M) was kept under stirring at 70 ° C for 2h. The obtained precipitation was separated and washed several times by centrifugation (4500 rpm, t = 15 min), then was heated at 60 ° C overnight. The resulting ZnO_2 powder was also calcinated at the same range of temperature from 400°C to 600°C to obtain finally ZnO mentioned, ZnP4T, ZnP5T, and ZnP6T, respectively.

2.3. Catalysts Characterization

For the structural analyses, X-ray Diffraction (XRD) was performed using an A25 Bruker D8 Advance diffractometer with Cu-Kα radiation. Crystallite size was calculated using Debye Scherer's equation:

$$D = \frac{K}{\beta cos\theta}\ \lambda.$$

Where D is the crystallite size, β is the full width at half-maximum, λ is the wavelength of X-ray radiation, θ is the Bragg angle, and K is taken as 1. The catalysts' structures were measured using a Micromeritics ASAP 2020 analyzer. Nitrogen adsorption/desorption isotherm at −196°C was performed and the Brunauer-Emmett-Teller (BET) method was used to determine the specific surface areas. Transmission Electron Microscopy (TEM) was carried out to determine the morphology of the samples using a JEOL 2010 (200 kV) microscope. The optical properties of ZnO samples were carried out using an AvaSpec-2048 Fiber Optic UV-Vis Spectrometer with an asymmetrical Czerny-Turner design. Spectra were recorded from 250 to 800 nm using a 2048 pixel CCD detector array. Raman experiments were performed using Horiba Jobin Yvon LabRAM-HR equipment. A spectral resolution of 4 /cm was achieved while a 514 nm from an Ar^+ ion laser and a CCD detector cooled at −75°C were used. X-ray photoelectron spectroscopy (XPS) studies were carried out using a KRATOS Axis Ultra DLD spectrometer equipped with a hemispherical analyzer operating at fixed pass energy of 40 eV. A 225 W monochromatic source (1486.6 eV) was used. Curve fitting was done using mixed Gaussian and Lorentzian functions for line shaping after-treatment of the background using a Shirley-type baseline (casaXPS software, version 2.3.23). EPR assays were all carried out at room temperature using a Bruker E500 spectrometer operating at X-band (9.34 GHz), sensitive cavity, with 100 kHz modulation frequency. The instrument settings were as follows: microwave power; 22mW; modulation amplitude; 1 G. The charge-carrier lifetimes were determined by microwave absorption experiments using the TRMC method. The incident microwaves were generated by a Gunn diode of the K_α band at 30 GHz. The pulsed light source was an OPO laser (EKSPLA, NT342B) tunable from 225 to 2000 nm. It delivers 8 ns fwmh pulses with a frequency of 10 Hz. The light energy density received by the sample was 0.9 mJ cm^{-2} at 350 nm.

2.4. Photocatalytic experiments

Photocatalytic properties were assessed using a 50 mL Pyrex photoreactor with a side magnetic stirring, containing formic acid and phenol as the reactant model molecules for photo-degradation. 30 mL of formic acid (50 ppm) or phenol (20 ppm) solution containing ZnO catalyst at a concentration of 1 g/L was stirred in the dark for 30 min before UV irradiation to reach adsorption equilibrium conditions. Then, the suspensions were irradiated by a PL-L 18W lamp (Phillips) placed below the photoreactor, with a power set at 6 mW/cm². 500 µL were sampled at different irradiation times and

filtrated on MILLEX HVLP 0.45 µm hydrophilic filter (Millipore) before HPLC analysis. Formic acid analysis was performed by a VARIAN PROSTAR HPLC system with the automated sampler. A Coregel-87H3 column (300 mm x 7.8 mm – Concise Separations) was used, thermostated at 30°C. An H_2SO_4 (5.10^{-3} mol/L) mobile phase was used at a flow rate of 0.7 mL/min. For detection, a Prostar325 UV-Vis module was set at 210 nm. 1290 Infinity HPLC system (Agilent Technologies) was used for phenol analysis using a Nucleosil 250 x 4.6 mm 5 µm C18 column (Macherey-Nagel) thermostated at 40°C. The mobile phase was composed of 20% methanol and 80% of aqueous H_3PO_4 (1 mM, pH = 3). A PDA detector was used at the 210 nm wavelength.

3. Results and discussion

3.1. Characterizations of ZnO samples

3.1.1. X-ray diffraction, BET, and TEM studies

The XRD patterns of the different ZnO samples elaborated are shown in Figure1a, b, c. Typical diffraction peaks at 2θ = 31.58°, 34.34°, 36.31°, 47.35°, 56.62°, 62.73°, 67.87° attributed respectively to (100), (002), (101), (102) (110), (103) and (112) planes, and corresponding to hexagonal Wurtzite structure of ZnO (JCPDS 36-1451), are present whatever the precursor or treatment. In the case of $Zn(CH_3CO_2)_2$, a UV pre-treatment was done on the ZnO sample only dried at 60°C in trying to maintain a high surface area and eliminate the acetate not completely removed at this temperature. Samples prepared from $Zn(CH_3CO_2)_2$ and calcined at different temperatures or irradiated under UV-A are presented in figure1.a. After UV treatment and in absence of calcination (ZnA60-UV), other additional peaks marked by stars on the XRD pattern are detected, probably due to the formation of organic compounds issued from the decomposition of $Zn(CH_3CO_2)_2$ by photolysis or photocatalysis. After calcination at 400°C (ZnA4T-UV), these impurities disappear, Without UV pre-treatment, and with annealing at 400°C, 500°C, and 600°C, a clear sharpening of diffraction peaks are observed attributed to the increase of crystallite size and the improvement of the crystallinity. Crystallite size was calculated by the X-ray line broadening method using Scherer's equation [39]. Table 1 presents the crystallite size and BET surface areas of the samples. As shown, the average crystallite sizes of the ZnO nanoparticles prepared from $Zn(CH_3CO_2)_2$ increased from 8 nm to 39 nm on heating from 60° C to 600° C in good agreement with the decrease of BET surface area. The specific surface area of 88 m^2/g obtained for the sample only dried at 60°C, decreased to 34 m^2/g, then 17 m^2/g and 10 m^2/g after respective calcinations at 400°C, 500°C, or 600°C.

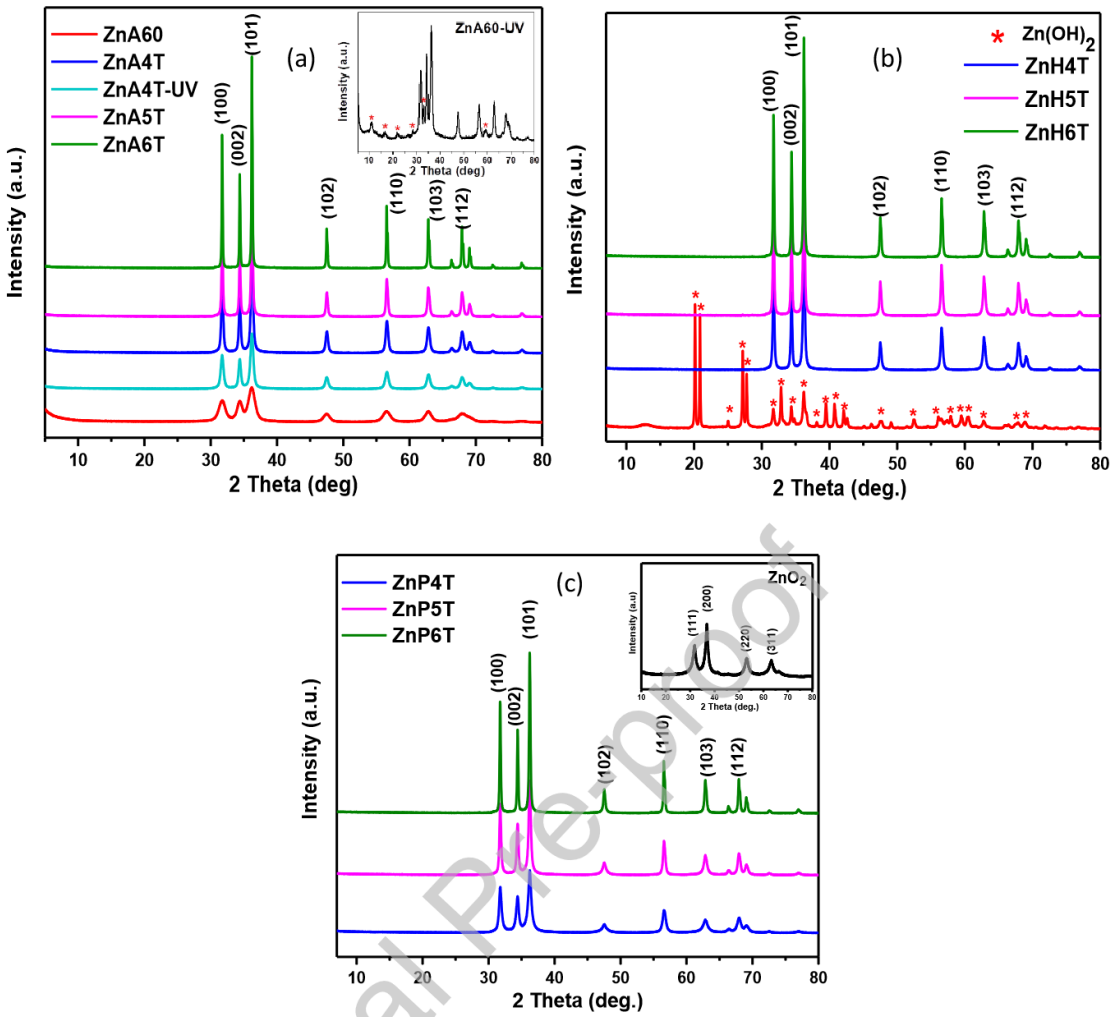

Fig. 1. XRD pattern of ZnO samples (a) from $Zn(CH_3CO_2)_2$ precursor calcined at different temperatures or UV treated, (b) using $Zn(OH)_2$ as a precursor calcined at different temperatures, and, (c) by thermal conversion of ZnO_2.

A similar effect of the calcination temperature is also observed using $Zn(OH)_2$ or ZnO_2 as a precursor (Figure 1b and 1c). A complete conversion of $Zn(OH)_2$ or ZnO_2 to a pure phase of Wurtzite structure is obtained at 400°C and as previously observed for the precursor $Zn(CH_3CO_2)_2$, an increase of annealing from 400°C to 600°C favors the growth of particle size and decrease the surface area.

Tab. 1. Average crystallite size and BET surface area of ZnO samples.

	ZnA	ZnA	ZnA	ZnA	ZnA UV	ZnA UV	ZnH	ZnH	ZnH	ZnP	ZnP	ZnP
T (°C)	**60**	**400**	**500**	**600**	**60**	**400**	**400**	**500**	**600**	**400**	**500**	**600**
Crystallite size (nm)	8	19	27	39	7	14	23	27	32	14	20	31
BET (m^2/g)	88	34	17	10	134	37	17	13	10	17	13	10

Besides the variation in crystallite sizes, according to the results from Transmission Electron Microscopy (TEM) presented in Figure 2, the nature of the precursor by using these protocols does not affect the morphology of the resulting ZnO. In all the cases, a spherical morphology is shown and the average particle size is between ~14 nm and ~27 nm. However, the nature of the precursor and the calcination temperature, play a role in the relative intensity of the XRD peaks, identifying variation in the growth orientation of the crystallites [40]. In our conditions, except for ZnPxT, the ratios between <100>/<101> peaks are equivalent whatever the calcination temperatures and for the different precursors, the growth of the <002> plane decreases with the increase in calcination temperature for both precursors. On the opposite, the growth of the <002> is favored under UV.

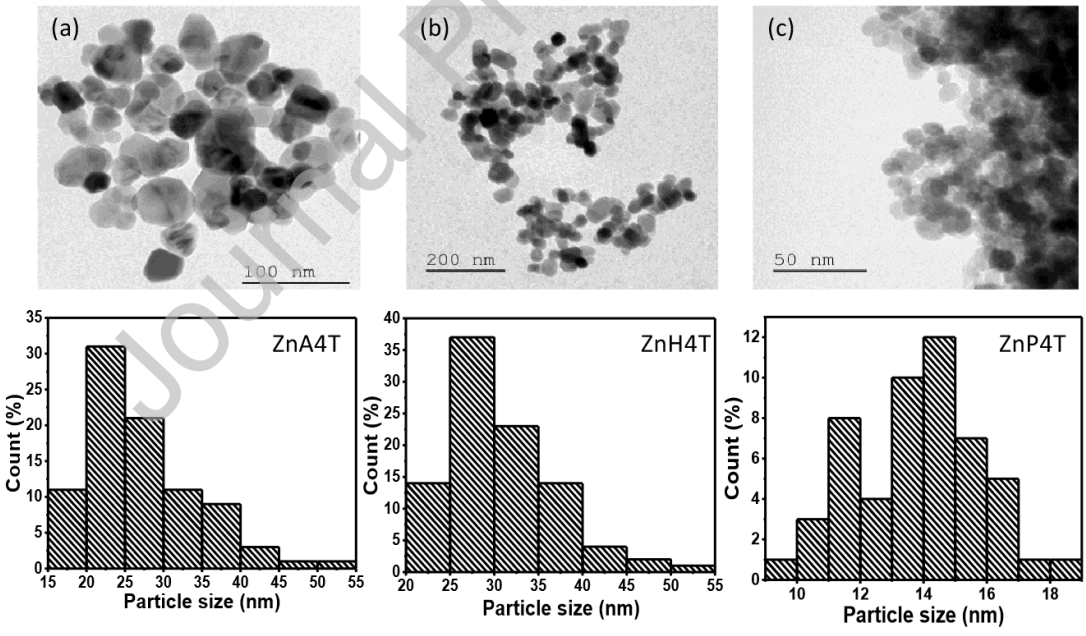

Fig.2. TEM images of ZnO samples prepared from Zinc Acetate (a), Zinc Hydroxide (b), and Zinc Peroxide (c), calcined at 400°C. (The Particle Size distribution based on TEM data is presented in all the cases).

Tab. 2. The ratio between diffraction peaks 100, 002, and 101 for ZnO at different temperatures

	ZnA	ZnA	ZnAUV	ZnA	ZnA	ZnH	ZnH	ZnH	ZnP	ZnP	ZnP
T (°C)	**60**	**400**	**400**	**500**	**600**	**400**	**500**	**600**	**400**	**500**	**600**
(100/101)	0,63	0,64	0.62	0,63	0,63	0,64	0,63	0,65	0.79	0.75	0.70
(002/100)	0,97	0,80	0.88	0,71	0,70	0,79	0,76	0,74	0.80	0.72	0.75
(002/101)	0,61	0,51	0.54	0,45	0,44	0,50	0,48	0,48	0.63	0.54	0.52

3.1.2. UV-Visible

The bandgap energies for the home-made ZnO samples were investigated by UV−visible diffuse reflectance spectroscopy using the Kubelka-Munk method considering direct bandgap transition for ZnO: $(\alpha h\nu)^2$ versus (hv) where α is the absorption coefficient and hv is the photon energy [41,42]. The optical energy gap Eg for materials elaborated at different temperatures from $Zn(CH_3CO_2)_2$, $Zn(OH)_2$, and ZnO_2, are presented respectively in Fig. 3a, b, and c. Values of bandgap are reported in Table 3. They are situated between 3.2 eV and ~3 eV for ZnA and ZnH in agreement with the values reported in the literature [43–45]. However, in the case of ZnP, the values are lower (2.9 eV). With $Zn(CH_3CO_2)_2$ precursor, a slight modification of the bandgap with the calcination temperature seems to occur, which can be attributed to some morphological changes, such as the changes in particle size of ZnO as mentioned in other studies or to defect states, appearing with calcination, and behaving like electron collecting centers [27]. According to Fig. 3b, the ZnO samples prepared from $Zn(OH)_2$ and calcined at different temperatures exhibited the same behavior and their optical band gap energy was situated at 3.15 eV for all ZnH samples independently of the calcination temperature. The same behavior was observed with samples prepared from ZnO_2 (Figure 3. c) but with a more intense yellow color and bandgap energy decreased to 2.9 eV, with the sample treated at 400°C then, 2.98 eV, and 3 eV, at 500°C and 600°C, respectively. In literature, this behavior has been attributed to the existence of oxygen vacancies leading to the insertion of defect levels within the bandgap of ZnO [46,47].

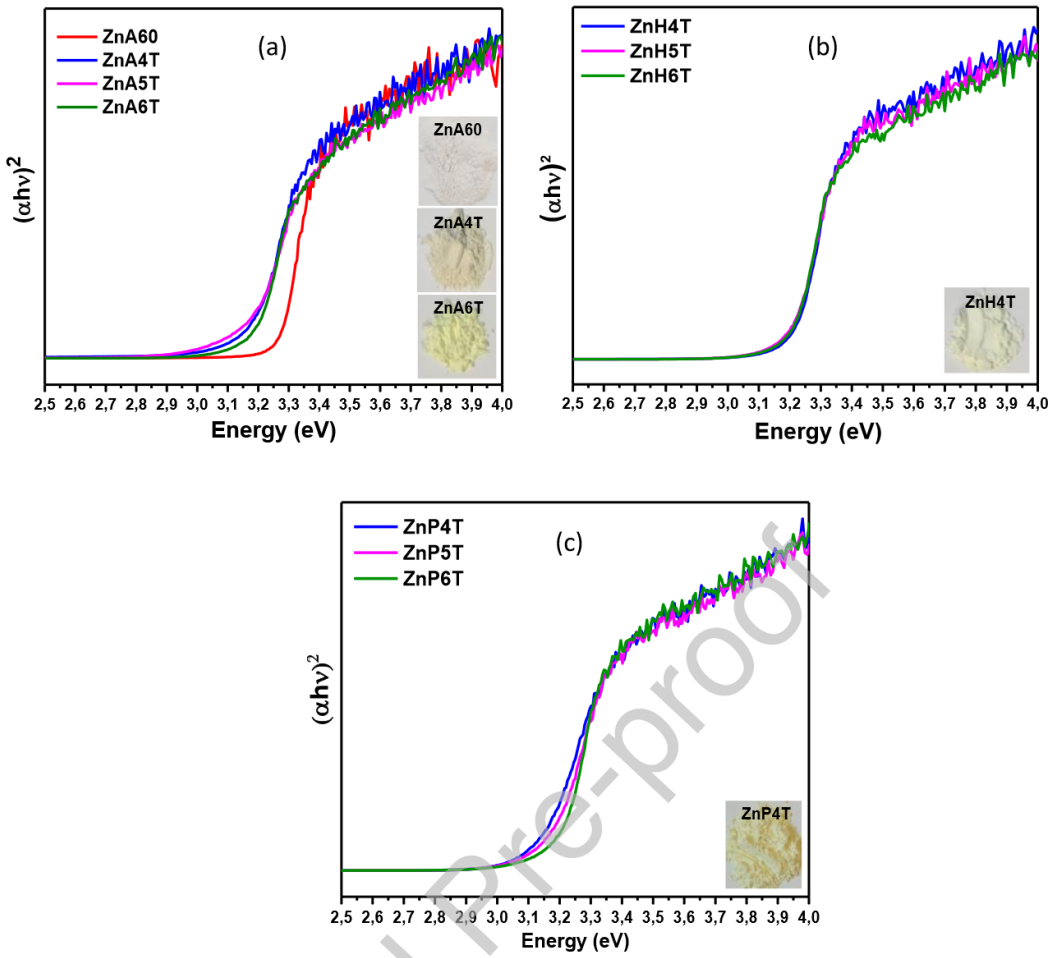

Fig.3. The energy band gap of homemade ZnO prepared from (a) $Zn(CH_3CO_2)_2$, (b) $Zn(OH_2)$, and (c) ZnO_2 at different calcination temperatures.

Tab. 3. Bang gap values of ZnO samples from different precursors.

Samples	ZnA60	ZnA4T	ZnA5T	ZnA6T	ZnH4T	ZnH5T	ZnH6T	ZnP4T	ZnP5T	ZnP6T
The bandgap (eV)	3.18	3.10	3.08	3.11	3. 15	3. 15	3.15	2.9	2.98	3

3.1.3. Raman spectroscopy

The Raman spectra of the prepared ZnO samples are shown in Figure 4. Fig.4a presents the spectrum of samples prepared from $Zn(CH_3CO_2)_2$ as a precursor. As shown, the un-calcined samples, with and without UV treatment, exhibit additional bands not identified at 147 cm^{-1}, 734 cm^{-1}, and 930 cm^{-1} which may be related to the presence of impurities. On the other hand, the samples elaborated with $Zn(CH_3CO_2)_2$ treated at 400°C (with or without UV treatment), exhibit an excessive fluorescence that

masks the Raman signal. In this case, their spectra are not considered. For the samples calcined at 400°C prepared by using $Zn(OH)_2$ and ZnO_2, this phenomenon of excessive fluorescence was not observed. Whatever the precursor or the treatment (Fig.4), we can identify two strong typical Raman peaks appearing at 98 cm^{-1}, and 437 cm^{-1} assigned to first-order modes characteristic of ZnO Hexagonal Wurtzite structure [48,49], corresponding to E_2^{Low}, and E_2^{High} modes, and generated by Zn-Zn and O-O vibrations, respectively [50]. The band at 202 cm^{-1} and 330 cm^{-1} are attributed to the second-order mode of $2E_2^{Low}$ and E_2^{High} -E_2^{Low}, respectively [51,52]. On the other hand, an additional peak at around 580 cm^{-1} is observed. This signal corresponds to Zn-O stretching vibration and is recorded to (E_1^{Lo}) mode showing oxygen vacancies appearing in the ZnO crystal [53,54]. From these Raman analyses, we determined the intensity ratio of E_1^{Lo} / E_2^{High} which is related to oxygen defects distribution versus the crystallinity of the samples [27] (Table 4). The difference in the contribution of defects is observed between catalysts from different precursors at different calcination temperatures. It can be noticed that oxygen defects decrease with increasing calcination temperature in the case of ZnO_2, more important than with $Zn(CH_3CO_2)_2$ or $Zn(OH)_2$. The same behaviour has been observed in the literature using ZnO_2 as a precursor and has been attributed to the contribution of oxygen vacancies resulting from the decomposition of ZnO_2 [46]. The decrease of oxygen defects by increasing calcination temperature agrees with the decrease of yellow colour and the increase of bandgap highlighting the influence of oxygen vacancies on the formation of intermediate levels in the bandgap of the materials.

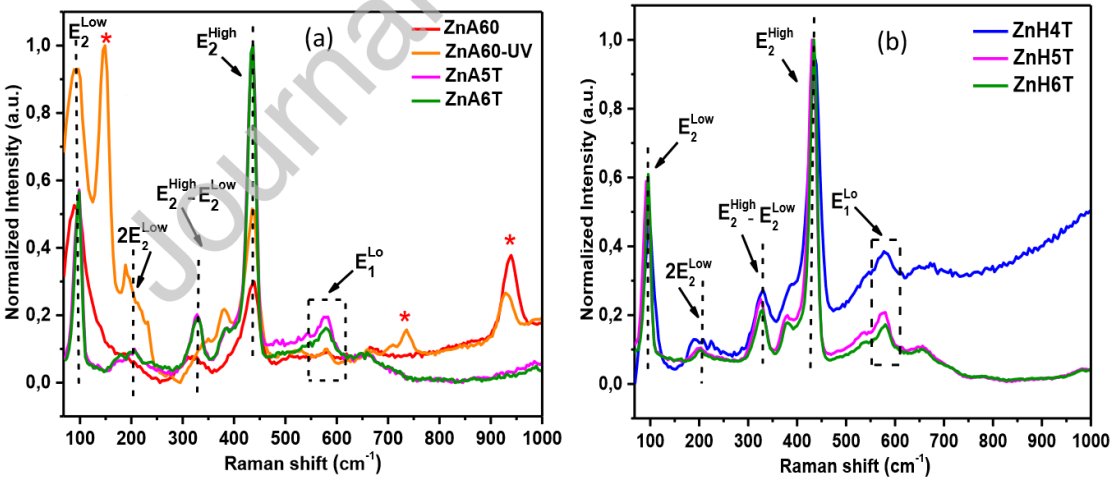

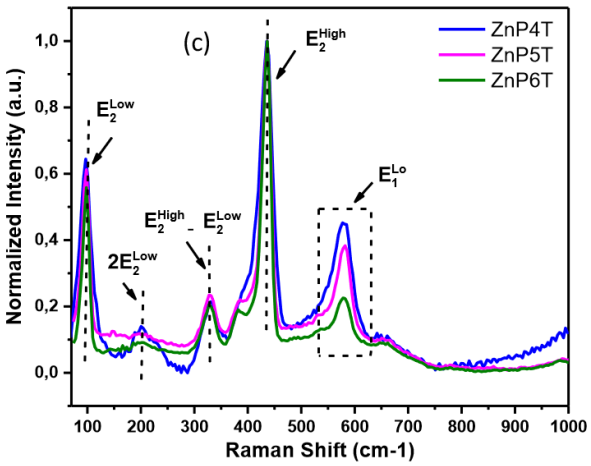

Fig.4. Normalized Raman spectra of prepared ZnO from (a) $Zn(CH_3CO_2)_2$, (b) $Zn(OH)_2$ and (c) ZnO_2, calcined at different temperatures.

Tab. 4. The intensity of E_1^{Lo} mode and the Intensity Ratio of (E_1^{Lo}/ E_2^{High}) modes of ZnO samples were prepared from different precursors and, calcined at different temperatures.

	ZnA5T	ZnA6T	ZnH4T	ZnH5T	ZnH6T	ZnP4T	ZnP5T	ZnP6T
I (E_1^{Lo})	0.06	0.05	0.06	0.06	0.05	0.31	0.23	0.10
I (E_1^{Lo})/ I (E_2^{High})	0.07	0.06	0.07	0.07	0.06	0.38	0.28	0.12

3.1.4. X-ray photoelectron spectra

The High-resolution XPS spectra of the ZnO samples from different precursors are presented in Figure 5. As shown, the O1s spectra of all the spectra are asymmetric and can be deconvolved into two major species centered at the banding energy of 529.8 and 531.4 eV, respectively. The O1s peak at ~530 eV is attributed to the Lattice oxygen ions in the Wurtzite ZnO structure. However, the peak at ~ 531 eV originates from oxygen vacancies implying the presence of deficient regions on the surface of ZnO [47]. The results presented confirm the presence of oxygen vacancies in all samples.

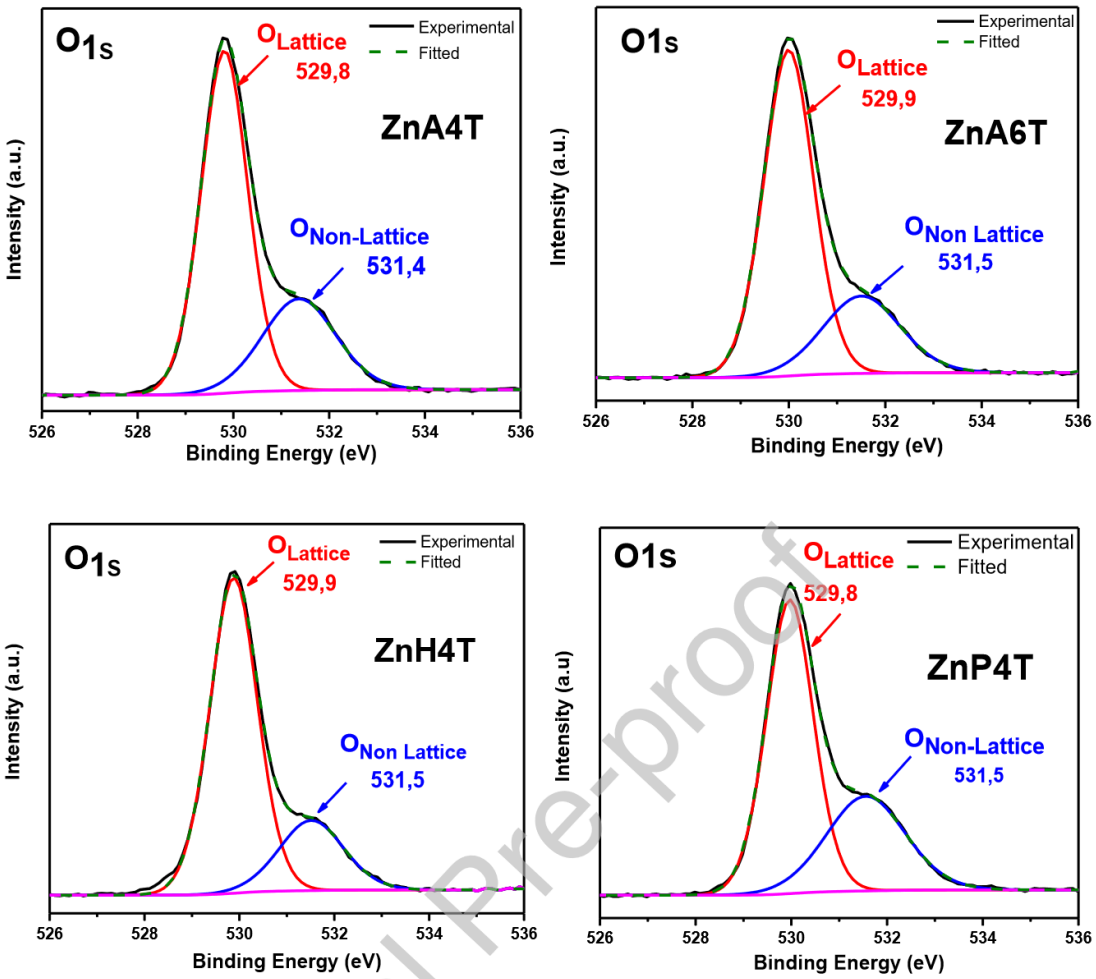

Fig. 5. X-ray photoelectron spectra (XPS) of O_{1s} signals for ZnO samples from different precursors.

3.1.5. Electron Paramagnetic Resonance (EPR)

EPR was used to characterize defects present in the structure of ZnO nanoparticles. Figure 6 shows the results obtained for ZnO samples prepared from different precursors and presenting the same surface areas to obtain the same degree of defect density. The observed signals were recorded at room temperature and were analyzed in air. The EPR spectra are compared for samples showing the same surface area. In all the cases and for all the samples, there is a first-order EPR signal at g=1.96 in good agreement with the value indicated previously in the literature [55,56]. As reported, this signal is assigned to electrons in delocalized states in the conduction band of ZnO, and oxygen vacancies are the origin centers [57,58]. An additional paramagnetic resonance is detected at g>2 and is attributed to zinc vacancies centers [57,59,60]. A single line close to the g-factor of the free electron (g~2.004) corresponding to the presence of non-distorted zinc vacancies is strong in the case of acetate precursor and weak for the two others (Figure 6 (a)). These zinc vacancies decrease after

thermal treatment (Figure 6 (b) and (c)), showing the correlation between the loss of zinc vacancies, the increase in crystallinity and crystallite size, and decrease in surface area. Additive signals are observed at higher g values, especially for the peroxide precursor. This center results in a more distorted environment [61] and probably O-centred radical species as previously observed in the literature [32].

We note that ZnO prepared from zinc peroxide (with a surface area of 17, 13, and, 10 m^2/g), has the most important number of defects, compared to the samples prepared from zinc acetate and zinc hydroxide. Overall, ZnO issued from zinc hydroxide presents the minimum number of defects. These results show that both kinds of defects strongly depend on the nature of precursors used to elaborate ZnO nanoparticles, which has consequently an effect on the activity of electrons under UV and their accessibility to the active sites related to defects. This gives an insight in the origin of differences in respective photocatalytic activities.

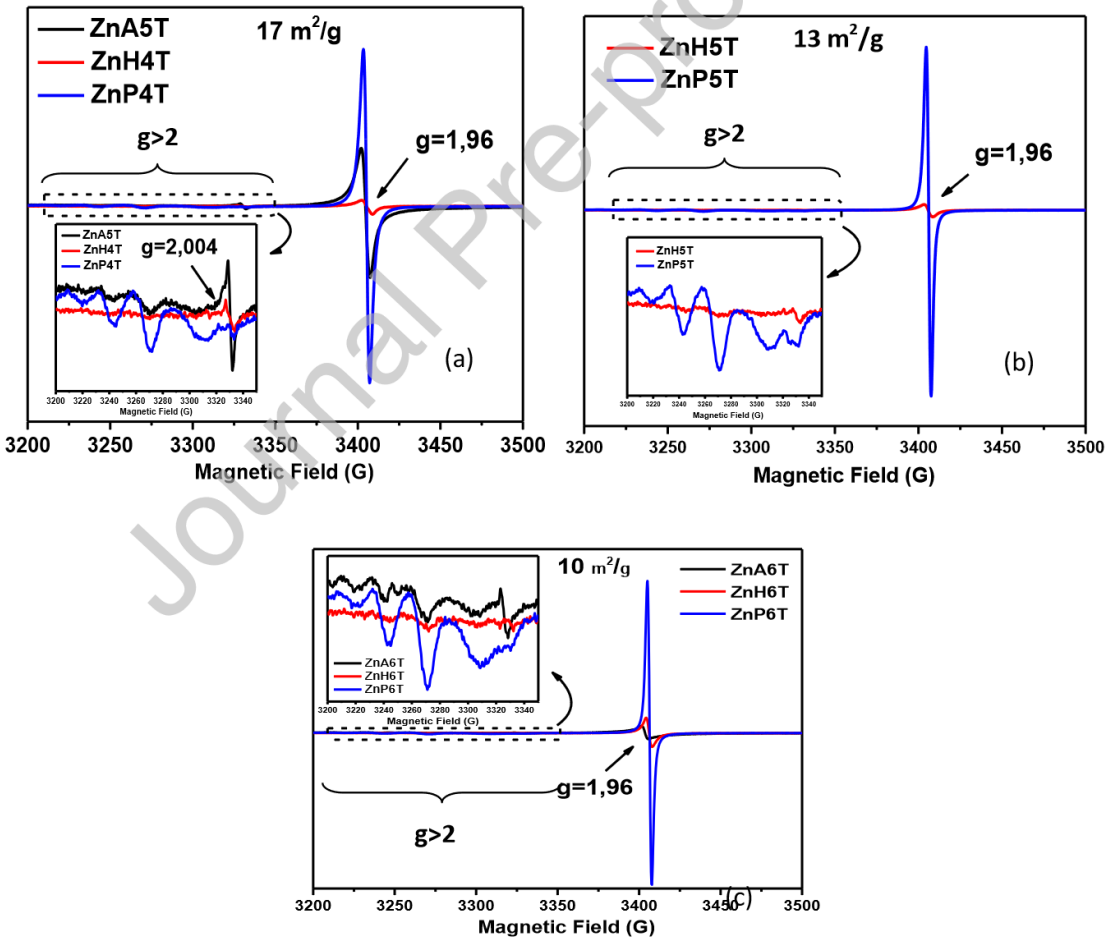

Fig. 6. Comparison of EPR spectra of ZnO prepared using different precursors and having a similar surface area of 17 m^2/g (a), 13 m^2/g (b), and 10 m^2/g (c).

3.1.6. Time-resolved microwave conductivity (TRMC)

Figure 7 presents the TRMC signals for the samples obtained from $Zn(CH_3CO_2)_2$ irradiated under UV or not and with or without calcination at 400°C. The main data provided by TRMC and given in table 5 are the maximum value of the signal (I_{max}), which indicates the number of charge carriers created by the pulse, including decay processes during the excitation by the laser (10 ns), and the decay ($I(t)$) due to the decrease of the excess electrons, either by recombination or by trapping processes. Concerning the decay, i.e. the lifetime of charge carriers, a short and a long range is usually analysed. The short-range decay, arbitrarily fixed up to 40 ns after the beginning of the pulse, represented by the I_{40ns}/I_{max} ratio, reflects fast processes, mainly recombination of charge carriers, a high value indicating a low ratio of fast recombination processes. Figure 7 shows clearly the great influence of thermal treatment on charge carriers. Both 4T (calcinated at 400°C) compounds ZnA4T and ZnA4T-UV present an important TRMC signal while no signal is detected without calcination. A TRMC signal is observed when enough mobile charge carriers are created by the illumination. Large well-crystallized particles favour the generation of charge carriers [62]. On the opposite, small particles are not favourable to strong signals because they contain a lot of impurities and amorphous zones. The poor crystallinity can annihilate the TRMC signal because of high recombination during the laser pulse. The high crystallinity of large particles of 4T compounds explains clearly their large TRMC signals. The difference in crystallinity between calcinated and not calcinated compounds is evidenced by the analysis of peak broadening in XRD measurements in Fig. 1. The influence of UV pre-treatment is subtler. On Zn4T-UV, fewer charge carriers are created (lower I_{max}) than on Zn4T. But at the same time, fast recombination phenomena are reduced (higher I_{40ns}/I_{max}).

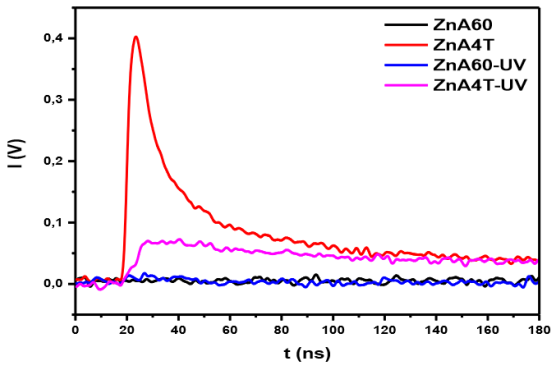

Fig. 7. TRMC signal of ZnO prepared from $Zn(CH_3CO_2)_2$before and after UV and thermal treatment at 400°C.

Tab. 5. TRMC parameters of ZnO prepared from $Zn(CH_3CO_2)_2$ at 365 nm.

Sample	I_{max} (V)	I_{40ns} (V)	I_{40ns}/I_{max}
ZnA4T	0.40	0.16	0.39
ZnA4T-UV	0.07	0.07	1.00

3.2. Photocatalytic properties for degradation of formic acid and phenol

The impact of the calcination temperature of ZnO has been studied on the degradation of two model pollutants, formic acid (FA) and phenol (Ph).

3.2.1. Impact of calcination temperature on ZnO prepared by using ($Zn(CH_3COO)_2$)

The impact of the calcination temperature on the disappearance of formic acid (FA) and Phenol (Ph) in presence of ZnO prepared by using Zn $(CH_3COO)_2$ is given in Fig.8. The disappearance rate of FA and Ph obtained under different temperatures with or without UV-pre-treatment together with their surface area are given in table 6.

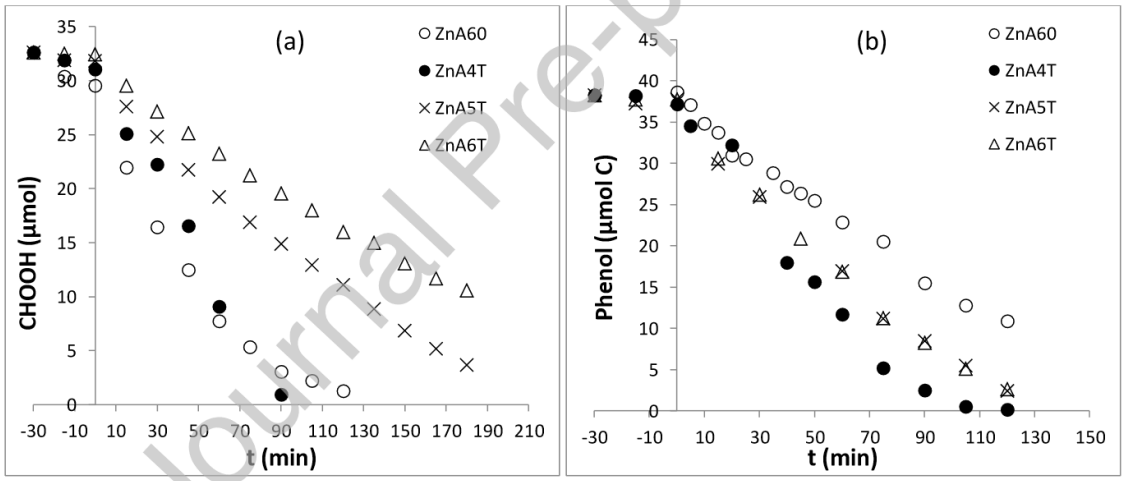

Fig. 8. Photocatalytic disappearance of formic acid (a) and phenol (b) in presence of ZnO prepared from $Zn(CH_3COO)_2$ and heated at different temperatures.

First of all, by using the precursor $Zn(CH_3COO)_2$, it can be noted that calcination is not necessary to obtain a photocatalytic activity in agreement with the results obtained by Akir et al [63] on the photocatalytic degradation of a dye using the same preparation and only a drying at 60°C. However, whereas the degradation of FA is important and not improved by calcination at 400°C, calcination at 400°C improves the rate of degradation of phenol by a factor of almost 2. Nevertheless, even after just a drying at 60°C, its activity is not negligible due to its crystallization at low temperature as observed by RX diffraction. The difference in behaviour observed between the rate of FA and Ph is

explained considering the presence of acetate remaining in the solid, released in the solution as acetic acid, and then degraded in competition with FA and Ph (Fig. 9). Indeed, it is observed that the photocatalytic degradation of generated acetic acid under UV light differs from the photocatalytic degradation of formic acid and phenol. Acetic acid released in the solution is simultaneously degraded with Phenol, whereas its degradation occurs only after the degradation of FA. This behavior underlined the importance of adsorption on the degradation when the organic precursor is used and showed that the presence of some impurities in photocatalyst is harmful in agreement with the work of Franco et al [35].

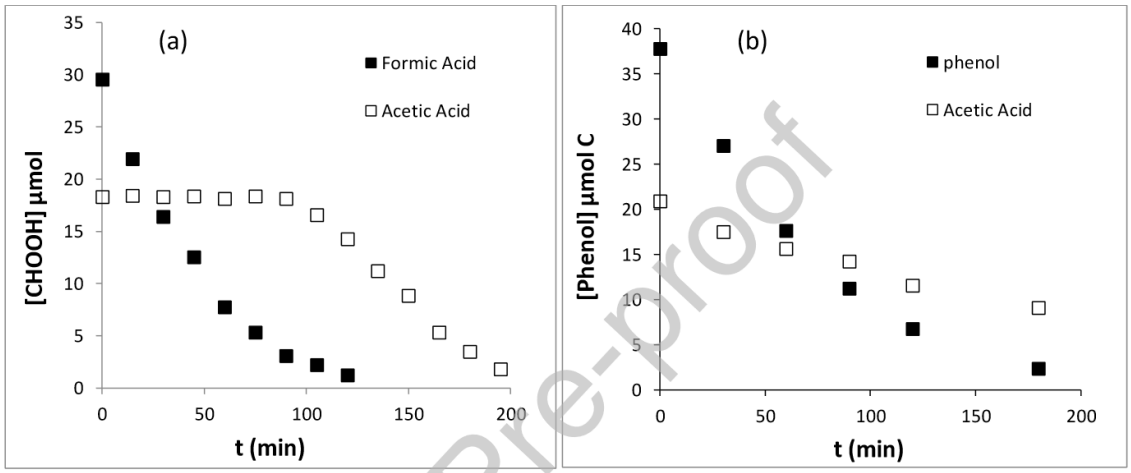

Fig. 9. Disappearance of (a) formic acid, and (b) phenol, in presence of ZnA-60 (Full Square) and disappearance of acetic acid release in the solution (Empty Square).

To verify that the presence of acetate, remaining in the materials, is at the origin of the different behavior between FA and Ph, two ways were tested to remove acetate in the materials. Calcination in the air at 400°C and UV treatment as already used for removing organic in the post-processing of TiO_2 based composites [64]. This treatment is used to remove organic impurities while maintaining a large surface area. As a result, the UV treatment although having allowed the elimination of all the acetic acid and the increase of the surface from 88 m^2/g to 134 m^2/g, a new unidentified phase is observed by XRD (Fig.1), explaining the decrease of FA and Ph disappearance. After calcination at 400°C, only the ZnO phase was detected but, whereas the calcination improves the disappearance rate of Ph, an important decrease in FA disappearance was observed (Fig. 10). In the absence of UV pre-treatment and after calcination in the air for 2h at 400°C, no acetic acid was detected and as forecast, no impact on FA disappearance was observed whereas an improvement of Ph disappearance occurs confirming our hypothesis. We noticed that the ZnO sample calcined at 400°C without UV pre-treatment is more active than this one pre-treated in agreement with TRMC

measurement. For non-adsorbing compounds such as phenol, TRMC signals can be related to the photocatalytic activity of the ZnO samples. It can help to understand the mechanisms [65].

Both ZnA4T and ZnA4T-UV compounds are the fastest to degrade phenol (Fig. 8.b and Fig. 10.b). This can be related to their high TRMC signals; it means their high crystalline quality allows enough long-time charge carrier to lead the phenol degradation. Zn4T-UV is slightly less active than Zn4T (Fig. 10.b) because it creates less charge carrier during illumination even if it generates less fast recombination.

On the opposite ZnA60 and ZnA60-UV are not very active because of their low amount of charge carriers available. Such a relationship cannot be drawn with adsorbing compounds like formic acid. In this case, during the photocatalytic mechanism, the surface reactions seem to take precedence over the charge carrier dynamics.

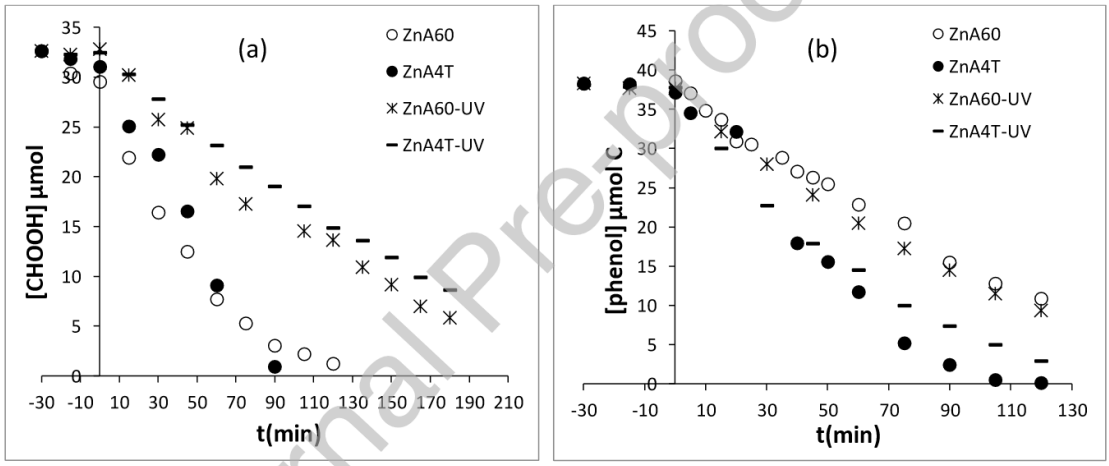

Fig. 10. The disappearance of FA (a), and Ph (b), after UV treatment and/or calcination at 400°C.

Tab. 6 Disappearance rate of FA and Ph, calcination temperature, and surface area of catalysts prepared by using $Zn(CH_3COO)_2$.

	T°C	S (m^2/g)	r(HCOOH) µmol-C/min	r(Phenol) µmol-C/min
ZnA60	60	88	0,35	0,25
ZnA4T	400	35	0,34	0,44
ZnA60-UV	60 after UV	134	0.20	0.26
ZnA4T-UV	400 after UV	37	0,13	0,36
ZnA5T	500	17	0,18	0,32
ZnA6T	600	10	0,15	0,32

Except for drying at 60°C where organic compounds are always present in the structure of the catalyst, for both pollutants, the impact of calcination temperature from 400°C to 600° has a negative impact on the disappearance rate (Tab.6, Fig.8). However, whereas an increase in the temperature at 600°C, continues to decrease the disappearance rate of FA, no impact was observed on the rate of Ph. The negative impact of calcination temperature should be related to the surface area of ZnO, which is more important in the case of FA degradation compared to Ph due to its chemical adsorption on oxide favoring the separation of charge by direct reaction with h^+ while Ph is weakly adsorbed and reacts with OH° [66].

3.2.2 Impact of calcination temperature on ZnO prepared by using inorganic precursors ($Zn(OH)_2$) and ZnO_2

Figure 11 represents the disappearance rate of FA and Ph as a function of the calcination temperature using $Zn(OH)_2$ and ZnO_2 as precursors. Table 7 gives the disappearance rates of the compounds obtained as well as their specific surface areas. No impact of the calcination temperature of $Zn(OH)_2$ between 400°C to 600°C can be observed on the disappearance rate of FA and Ph, whereas the surface area decreases from 17 to 10 m^2/g (Tab.7). On the other hand, by using ZnO_2 as a precursor, an increase in temperature from 400°C to 500°C has no impact on the disappearance rate of HCOOH and a slightly positive impact on the disappearance rate of Ph which increases significantly by increasing the calcination temperature at 600°C whereas the surface area decreases. Consequently, and contrary to the results obtained with $Zn(CH_3CO_2)_2$, these results show that BET surface area is not the only parameter to be considered to evaluate the photocatalytic activity of ZnO when a pure inorganic precursor of zinc hydroxide $Zn(OH)_2$ or peroxide ZnO_2 are used. Considering the particularities of ZnO to create various defects in the crystal structure, previously confirmed with XPS, Raman, and EPR characterizations, this may explain such behaviour, and provide a better understanding of the various pathways responsible for the different photocatalytic activities observed with ZnO.

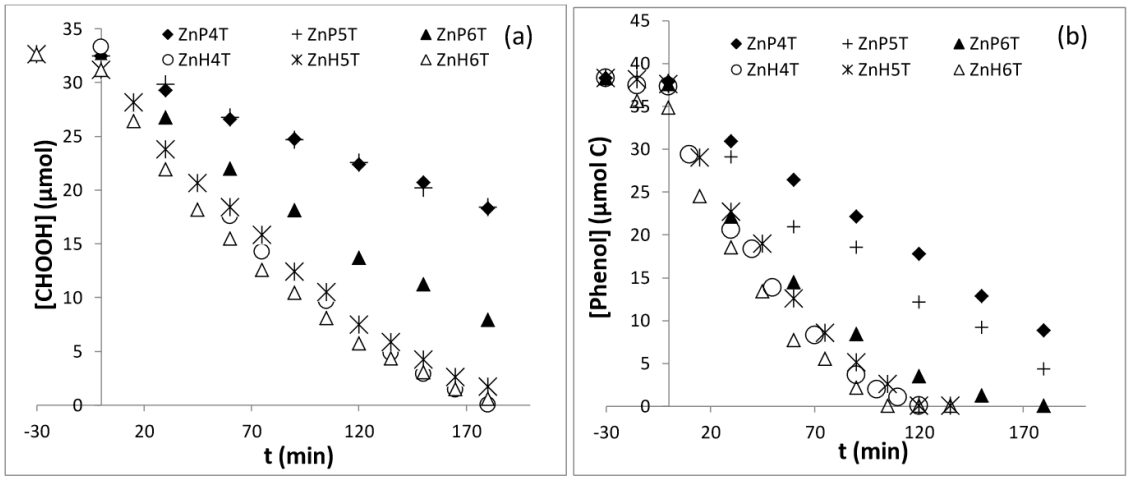

Fig. 11. degradation of FA (a), and Ph (b) as a function of time in presence of ZnO obtained at different calcination temperatures.

Tab. 7. Disappearance rate of FA and Ph, calcination temperature, and surface area of catalysts prepared by using $Zn(OH)_2$ and ZnO_2.

	T°C	S (m^2/g)	r(HCOOH) µmol-C/min	r(Phenol) µmol-C/min
ZnH4T	400	17	0.2	0.40
ZnH5T	500	13	0.2	0.40
ZnH6T	600	10	0.2	0.43
ZnP4T	400	17	0.08	0.16
ZnP5T	500	13	0.08	0.22
ZnP6T	600	10	0.14	0.38

3.2.3 Correlation between characterizations and photocatalytic activity: Surface area versus structural defects

By using $Zn(CH_3CO_2)_2$ as a precursor, the decrease of photocatalytic activity observed about calcination temperature is in good agreement with the study reported recently on the degradation of dyes using the same precursor [27]. In addition to the effect of surface area as already observed in the literature [25,26], but always in debate, the authors suggest that the presence of defects induced into the structure of ZnO could also be responsible for its photocatalytic efficiency indicating the difficulty to discriminate between the impact of these two parameters. In our case, we confirm, from EPR and XPS data, the presence of defects when using $Zn(CH_3CO_2)_2$ as a precursor. However, the surface area seems to be the dominant parameter that determines the efficiency and masks

probably other factors (Fig. S2). On the other hand, in presence of inorganic precursors, the role of oxygen vacancies may be highlighted by Raman spectroscopy considering the Intensity Ratio E1 (Lo)/E2 (High) (Fig. 12). With ZnO prepared from $Zn(OH)_2$, the surface decreases with an increase of the calcination temperature from 400°C to 600°C, while the disappearance rate remains similar. This is probably due to the presence of the same amount of oxygen vacancies which counterbalances the negative effect of the surface area, suggesting a detrimental effect on the photocatalyst efficiency due to the presence of defects in the ZnO structure. This phenomenon is clearly evident with the precursor ZnO_2 (ZnPxT). Whereas the surface area decreases with an increase in the calcination temperature the disappearance rate of FA and Ph increases strongly in agreement with the formation of fewer oxygen vacancies. The harmful impact of the presence of oxygen vacancies agrees with the work of [28,34] but disagrees with different publications [37,38]. The negative impact of the presence of oxygen vacancies observed in our publication is explained by the possibility to discriminate between the impact of surface area and the presence of oxygen vacancies which have in our cases opposite effects.

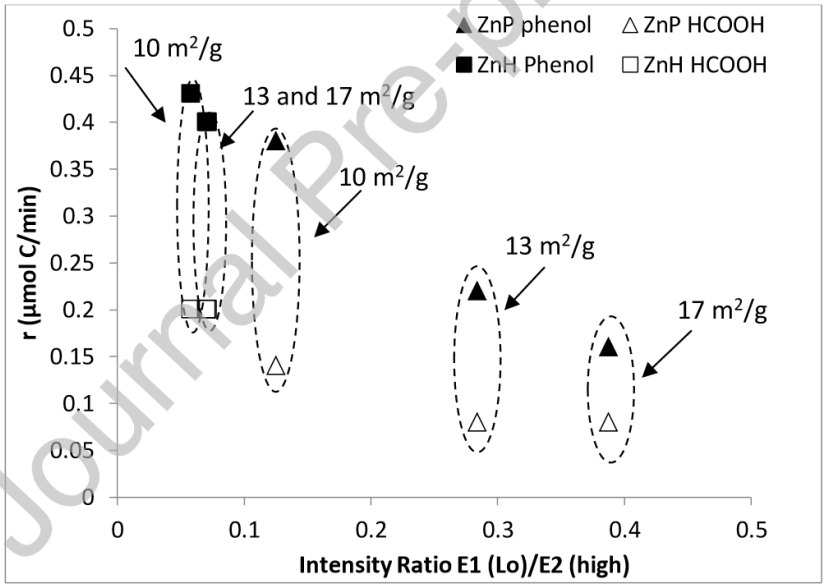

Fig. 12. Disappearance rate of phenol and HCOOH as a function of oxygen vacancies (Intensity Ratio of E1 (Lo)/E2 (high)) for the different ZnP and ZnH.

As shown, the amount of oxygen-related defects decreased with increasing calcination temperature from 400°C to 600°C in agreement with different works [31,46]. However, the authors conclude that the highest photocatalytic activity should be attributed to ZnO as it has the highest level of oxygen vacancies, without considering the surface area, which increases in parallel with an increase of oxygen defects. In the same way, several other publications working with Ag_3PO_4/ZnO [67], and

C_3N_4/ZnO [68], also conclude that higher oxygen vacancies favor the photocatalytic efficiency and show that the greater the oxygen deficiencies, the greater the surface area. So, in these different publications, it is not possible to discriminate between the impact of the surface area and oxygen vacancies. The harmful impact of the presence of oxygen vacancies is also confirmed by considering ZnO having a similar surface area prepared from these two inorganic precursors (Fig.12). The worst ZnO photocatalyst is obtained by using ZnO_2. Whereas its lower efficiency is attributed to the presence of oxygen defects, the presence of a little more (002) face in this material can also impact its efficiency. By using $Zn(CH_3CO_2)_2$, at a similar surface area, the use of this organic precursor seems to give a slightly less active photocatalytic material whereas an equivalent oxygen vacancy is determined by Raman analysis (Fig.S3). This behavior could be explained by the presence of more zinc vacancies for ZnO prepared by $Zn(CH_3CO_2)_2$ as observed with the signal at g>2 observed by electron paramagnetic resonance (EPR) (Fig. 6), in agreement with the study of Danilenko et al [31]. The negative impact of the presence of oxygen defects but also zinc defects can be explained considering the formation of intermediate levels between bandgap which serves as recombination centers [34].

Conclusion

A simple synthetic approach based on a thermal treatment and different zinc sources, $Zn(CH_3COO)_2$; $Zn(OH)_2$, and ZnO_2 have been employed to elaborate ZnO-based photocatalysts. Parameters such as impurities, surface area, oxygen and zinc vacancies, charge recombination, and photocatalytic activities for the degradation of phenol (Ph) and formic acid (FA) have been correlated for all these ZnO samples. A low temperature for the treatment of zinc acetate induces the release of organic impurities in water, harmful to the environment and photocatalysis. For all ZnO samples, an increase in the calcination temperature from 400°C to 600°C decreases the surface area. In the presence of zinc acetate as a precursor, an increase in calcination temperature decreases the oxidation efficacy of Ph and FA and seems to be correlated to the decrease of the surface area. Unfortunately, in this case, it is not possible to completely remove the impact of structural defects. However, by using $Zn(OH)_2$ and ZnO_2 as precursors, a high surface area does not mean a more efficient photocatalyst. interestingly, whereas the surface area decreases with increasing calcination temperature, an increase of the FA and Ph oxidation occurs. This result is explained considering the decrease of oxygen vacancies and emphasizes the harmful impact of these defects. The presence of zinc vacancies, evidenced by EPR spectroscopy, seems also counterproductive for photocatalytic properties, considering the disappearance rate of Ph and FA, for all ZnO owning the same surface area and the same oxygen vacancies. This result shows that both kinds of defects decreased the

photocatalytic activity of ZnO at similar surface areas, and favor the recombination rate of electron/hole. Overall, surface area and structural defects are complementary to each other, directly dependent on the choice of the precursor, and need to be considered in a strategy toward efficient ZnO photocatalyst.

Declaration of interests

The authors declare that they have no known competing financial interests or personal relationships that could have appeared to influence the work reported in this paper.

Funding information

The authors gratefully acknowledge the financial support from the Tunisian Ministry of Higher Education and Scientific Research, the University of Lyon 1 for collaboration, and the CNRS for receiving me.

Acknowledgment

The authors gratefully acknowledge the financial support from the Tunisian Ministry of Higher Education and Scientific Research, the University of Lyon 1 for collaboration, and the CNRS for receiving me.

References

[1] D. Friedmann, C. Mendive, D. Bahnemann, TiO2 for water treatment: parameters affecting the kinetics and mechanisms of photocatalysis, Appl. Catal. B Environ. 99 (2010) 398–406.

[2] S.-Y. Lee, S.-J. Park, TiO2 photocatalyst for water treatment applications, J. Ind. Eng. Chem. 19 (2013) 1761–1769.

[3] P. Pichat, C. Guillard, C. Maillard, L. Amalric, J.C. D'Oliveira, TiO2 photocatalytic destruction of water aromatic pollutants: intermediates; properties-degradability correlation; effects of inorganic ions and TiO2 surface area; comparisons with H2O2 processes, in: Photocatalytic Purification and Treatment of Water and Air, Eds. D.F. Ollis, H. Al-Ekabi, Elsevier, 1993, 207-223.

[4] K. Hayat, M.A. Gondal, M.M. Khaled, S. Ahmed, A.M. Shemsi, Nano ZnO synthesis by modified sol gel method and its application in heterogeneous photocatalytic removal of phenol from water, Appl. Catal. Gen. 393 (2011) 122–129.

[5] K.M. Lee, C.W. Lai, K.S. Ngai, J.C. Juan, Recent developments of zinc oxide based photocatalyst in water treatment technology: a review, Water Res. 88 (2016) 428–448.

[6] R. Qiu, D. Zhang, Y. Mo, L. Song, E. Brewer, X. Huang, Y. Xiong, Photocatalytic activity of polymer-modified ZnO under visible light irradiation, J. Hazard. Mater. 156 (2008) 80–85.

[7] J. Fenoll, E. Ruiz, P. Hellín, P. Flores, S. Navarro, Heterogeneous photocatalytic oxidation of cyprodinil and fludioxonil in leaching water under solar irradiation, Chemosphere. 85 (2011) 1262–1268.

[8] C. Lizama, J. Freer, J. Baeza, H.D. Mansilla, Optimized photodegradation of Reactive Blue 19 on TiO2 and ZnO suspensions, Catal. Today. 76 (2002) 235–246.

[9] M. Mrowetz, E. Selli, Photocatalytic degradation of formic and benzoic acids and hydrogen peroxide evolution in TiO2 and ZnO water suspensions, J. Photochem. Photobiol. Chem. 180 (2006) 15–22.

[10] A.H. Boonstra, C. Mutsaers, Adsorption of hydrogen peroxide on the surface of titanium dioxide, J. Phys. Chem. 79 (1975) 1940–1943.

[11] K. Sahel, L. Elsellami, I. Mirali, F. Dappozze, M. Bouhent, C. Guillard, Hydrogen peroxide and photocatalysis, Appl. Catal. B Environ. 188 (2016) 106–112.

[12] I. Daou, O. Zegaoui, A. Elghazouani, Physicochemical and photocatalytic properties of the ZnO particles synthesized by two different methods using three different precursors, Comptes Rendus Chim. 20 (2017) 47–54.

[13] M. Rezapour, N. Talebian, Comparison of structural, optical properties and photocatalytic activity of ZnO with different morphologies: Effect of synthesis methods and reaction media, Mater. Chem. Phys. 129 (2011) 249–255.

[14] R. Saravanan, V.K. Gupta, V. Narayanan, A. Stephen, Comparative study on photocatalytic activity of ZnO prepared by different methods, J. Mol. Liq. 181 (2013) 133–141.

[15] L. Xu, Y.-L. Hu, C. Pelligra, C.-H. Chen, L. Jin, H. Huang, S. Sithambaram, M. Aindow, R. Joesten, S.L. Suib, ZnO with different morphologies synthesized by solvothermal methods for enhanced photocatalytic activity, Chem. Mater. 21 (2009) 2875–2885.

[16] D. Li, H. Haneda, Morphologies of zinc oxide particles and their effects on photocatalysis, Chemosphere. 51 (2003) 129–137.

[17] S. Thakur, S. Neogi, A.K. Ray, Morphology-controlled synthesis of ZnO nanostructures for caffeine degradation and Escherichia coli inactivation in water, Catalysts. 11 (2021) 63.

[18] L. Zhang, Y.-J. Zhu, ZnO micro-and nano-structures: microwave-assisted solvothermal synthesis, morphology control and photocatalytic properties, Appl. Phys. A. 97 (2009) 847–852.

[19] Y. Chen, H. Zhao, B. Liu, H. Yang, Charge separation between wurtzite ZnO polar ${$0 0 1$}$ surfaces and their enhanced photocatalytic activity, Appl. Catal. B Environ. 163 (2015) 189–197.

[20] C. Li, H. Zhou, S. Yang, L. Wei, Z. Han, Y. Zhang, H. Pan, Preadsorption of O2 on the exposed (001) facets of ZnO nanostructures for enhanced sensing of gaseous acetone, ACS Appl. Nano Mater. 2 (2019) 6144–6151.

[21] E.S. Jang, J.-H. Won, S.-J. Hwang, J.-H. Choy, Fine tuning of the face orientation of ZnO crystals to optimize their photocatalytic activity, Adv. Mater. 18 (2006) 3309–3312.

[22] Y. Yamaguchi, M. Yamazaki, S. Yoshihara, T. Shirakashi, Photocatalytic ZnO films prepared by anodizing, J. Electroanal. Chem. 442 (1998) 1–3.

[23] G.R. Li, T. Hu, G.L. Pan, T.Y. Yan, X.P. Gao, H.Y. Zhu, Morphology- function relationship of ZnO: polar planes, oxygen vacancies, and activity, J. Phys. Chem. C. 112 (2008) 11859–11864.

[24] L. Wolski, J.E. Whitten, I. Sobczak, M. Ziolek, The effect of the preparation procedure on the morphology, texture and photocatalytic properties of ZnO, Mater. Res. Bull. 85 (2017) 35–46.

[25] N.M. Flores, U. Pal, R. Galeazzi, A. Sandoval, Effects of morphology, surface area, and defect content on the photocatalytic dye degradation performance of ZnO nanostructures, RSC Adv. 4 (2014) 41099–41110.

[26] L. Jing, Z. Xu, X. Sun, J. Shang, W. Cai, The surface properties and photocatalytic activities of ZnO ultrafine particles, Appl. Surf. Sci. 180 (2001) 308–314.

[27] P. Nandi, D. Das, Photocatalytic degradation of Rhodamine-B dye by stable ZnO nanostructures with different calcination temperature induced defects, Appl. Surf. Sci. 465 (2019) 546–556.

[28] V. Gurylev, T.P. Perng, Defect engineering of ZnO: Review on oxygen and zinc vacancies, J. Eur. Ceram. Soc. 41 (2021) 4977–4996.

[29] T.K. Le, T.M.T. Nguyen, H.T.P. Nguyen, T.K.L. Nguyen, T. Lund, H.K.H. Nguyen, T.K.X. Huynh, Enhanced photocatalytic activity of ZnO nanoparticles by surface modification with KF using thermal shock method, Arab. J. Chem. 13 (2020) 1032–1039.

[30] H. Zhang, Z. Tao, W. Xu, S. Lu, F. Yuan, First-principles study of dopants and defects in S-doped ZnO and its effect on photocatalytic activity, Comput. Mater. Sci. 58 (2012) 119–124.

[31] I. Danilenko, O. Gorban, P. Maksimchuk, O. Viagin, Y. Malyukin, S. Gorban, G. Volkova, V. Glasunova, M.G. Mendez-Medrano, C. Colbeau-Justin, T. Konstantinova, S. Lyubchyk, Photocatalytic activity of ZnO nanopowders: The role of production techniques in the formation of structural defects, Catal. Today. 328 (2019) 99–104.

[32] J. Wang, R. Chen, L. Xiang, S. Komarneni, Synthesis, properties and applications of ZnO nanomaterials with oxygen vacancies: A review, Ceram. Int. 44 (2018) 7357–7377.

[33] J. Wang, R. Chen, Y. Xia, G. Wang, H. Zhao, L. Xiang, S. Komarneni, Cost-effective large-scale synthesis of oxygen-defective ZnO photocatalyst with superior activities under UV and visible light, Ceram. Int. 43 (2017) 1870–1879.

[34] D. Chen, Z. Wang, T. Ren, H. Ding, W. Yao, R. Zong, Y. Zhu, Influence of Defects on the Photocatalytic Activity of ZnO, J. Phys. Chem. C. 118 (2014) 15300–15307.

[35] Franco, Sacco, De Marco, Vaiano, Zinc Oxide Nanoparticles Obtained by Supercritical Antisolvent Precipitation for the Photocatalytic Degradation of Crystal Violet Dye, Catalysts. 9 (2019) 346.

[36] T.K. Le, T.L. Nguyen, C.N. Hoang, D.K.A. Nguyen, T. Lund, H.K.H. Nguyen, T.K.X. Huynh, Formation of surface defects by thermal shock method for the improved photocatalytic activity of ZnO nanoparticles, J. Asian Ceram. Soc. 8 (2020) 193–202.

[37] Y.-H. Kim, S. Kim, K. Kim, C. Kim, J.H. Jang, Y.-M. Kim, H. Lee, Multiscale probing of the influence of the defect-induced variation of oxygen vacancies on the photocatalytic activity of doped ZnO nanoparticles, J. Mater. Chem. A. 8 (2020) 25345–25354.

[38] Q. Zhang, M. Xu, B. You, Q. Zhang, H. Yuan, K. Ostrikov, Oxygen Vacancy-Mediated ZnO Nanoparticle Photocatalyst for Degradation of Methylene Blue, Appl. Sci. 8 (2018) 353.

[39] N.W. Gregory, Elements of X-Ray Diffraction., J. Am. Chem. Soc. 79 (1957) 1773–1774.

[40] R. Romero, D. Leinen, E.A. Dalchiele, J.R. Ramos-Barrado, F. Martín, The effects of zinc acetate and zinc chloride precursors on the preferred crystalline orientation of ZnO and Al-doped ZnO thin films obtained by spray pyrolysis, Thin Solid Films. 515 (2006) 1942–1949.

[41] M. Kahouli, A. Barhoumi, A. Bouzid, A. Al-Hajry, S. Guermazi, Structural and optical properties of ZnO nanoparticles prepared by direct precipitation method, Superlattices Microstruct. 85 (2015) 7–23.

[42] M. Caglar, S. Ilican, Y. Caglar, F. Yakuphanoglu, Electrical conductivity and optical properties of ZnO nanostructured thin film, Appl. Surf. Sci. 255 (2009) 4491–4496.

[43] V. Srikant, D.R. Clarke, On the optical band gap of zinc oxide, J. Appl. Phys. 83 (1998) 5447–5451.

[44] M.M. Ba-Abbad, A.A.H. Kadhum, A. Bakar Mohamad, M.S. Takriff, K. Sopian, The effect of process parameters on the size of ZnO nanoparticles synthesized via the sol–gel technique, J. Alloys Compd. 550 (2013) 63–70.

[45] S.S. Kumar, P. Venkateswarlu, V.R. Rao, G.N. Rao, Synthesis, characterization and optical properties of zinc oxide nanoparticles, Int. Nano Lett. 3 (2013) 1-6.

[46] J. Wang, Z. Wang, B. Huang, Y. Ma, Y. Liu, X. Qin, X. Zhang, Y. Dai, Oxygen Vacancy Induced Band-Gap Narrowing and Enhanced Visible Light Photocatalytic Activity of ZnO, ACS Appl. Mater. Interfaces. 4 (2012) 4024–4030.

[47] Y. Tang, H. Zhou, K. Zhang, J. Ding, T. Fan, D. Zhang, Visible-light-active ZnO via oxygen vacancy manipulation for efficient formaldehyde photodegradation, Chem. Eng. J. 262 (2015) 260–267.

[48] T.C. Damen, S.P.S. Porto, B. Tell, Raman Effect in Zinc Oxide, Phys. Rev. 142 (1966) 570–574.

[49] C.A. Arguello, D.L. Rousseau, S.P.S. Porto, First-Order Raman Effect in Wurtzite-Type Crystals, Phys. Rev. 181 (1969) 1351–1363.

[50] J. Zhao, L. Wang, X. Yan, Y. Yang, Y. Lei, J. Zhou, Y. Huang, Y. Gu, Y. Zhang, Structure and photocatalytic activity of Ni-doped ZnO nanorods, Mater. Res. Bull. 46 (2011) 1207–1210.

[51] J.M. Calleja, M. Cardona, Resonant Raman scattering in ZnO, Phys. Rev. B. 16 (1977) 3753–3761.

[52] Y. Song, S. Zhang, C. Zhang, Y. Yang, K. Lv, Raman Spectra and Microstructure of Zinc Oxide irradiated with Swift Heavy Ion, Crystals. 9 (2019) 395.

[53] R. Cuscó, E. Alarcón-Lladó, J. Ibáñez, L. Artús, J. Jiménez, B. Wang, M.J. Callahan, Temperature dependence of Raman scattering in ZnO, Phys. Rev. B. 75 (2007) 165-202.

[54] H. Razavi-Khosroshahi, K. Edalati, J. Wu, Y. Nakashima, M. Arita, Y. Ikoma, M. Sadakiyo, Y. Inagaki, A. Staykov, M. Yamauchi, Z. Horita, M. Fuji, High-pressure zinc oxide phase as visible-light-active photocatalyst with narrow band gap, J. Mater. Chem. A. 5 (2017) 20298–20303.

[55] P.H. Kasai, Electron Spin Resonance Studies of Donors and Acceptors in ZnO, Phys. Rev. 130 (1963) 989–995.

[56] W.K. Liu, K.M. Whitaker, A.L. Smith, K.R. Kittilstved, B.H. Robinson, D.R. Gamelin, Room-Temperature Electron Spin Dynamics in Free-Standing ZnO Quantum Dots, Phys. Rev. Lett. 98 (2007) 186804.

[57] K. Hoffmann, D. Hahn, Electron Spin Resonance of Lattice Defects in Zinc Oxide, Phys. Status Solidi A. 24 (1974) 637–648.

[58] J.J. Schneider, R.C. Hoffmann, J. Engstler, S. Dilfer, A. Klyszcz, E. Erdem, P. Jakes, R.A. Eichel, Zinc oxide derived from single source precursor chemistry under chimie douce conditions: formation pathway, defect chemistry and possible applications in thin film printing, J. Mater. Chem. 19 (2009) 1449-1457.

[59] A. Janotti, C.G. Van de Walle, Native point defects in ZnO, Phys. Rev. B. 76 (2007) 165202.

[60] N. Xuan Sang, N. Minh Quan, N. Huu Tho, N. Tri Tuan, T. Thanh Tung, Mechanism of enhanced photocatalytic activity of Cr-doped ZnO nanoparticles revealed by photoluminescence emission and electron spin resonance, Semicond. Sci. Technol. 34 (2019) 025013.

[61] A.L. Taylor, G. Filipovich, G.K. Lindeberg, Electron paramagnetic resonance associated with Zn vacancies in neutron-irradiated ZnO, Solid State Commun. 8 (1970) 1359–1361.

[62] S. Boujday, F. Wünsch, P. Portes, J.-F. Bocquet, C. Colbeau-Justin, Photocatalytic and electronic properties of TiO2 powders elaborated by sol–gel route and supercritical drying, Sol. Energy Mater. Sol. Cells. 83 (2004) 421–433.

[63] S. Akir, A. Barras, Y. Coffinier, M. Bououdina, R. Boukherroub, A.D. Omrani, Eco-friendly synthesis of ZnO nanoparticles with different morphologies and their visible light photocatalytic performance for the degradation of Rhodamine B, Ceram. Int. 42 (2016) 10259–10265.

[64] D. Grégori, I. Benchenaa, F. Chaput, S. Thérias, J.-L. Gardette, D. Léonard, C. Guillard, S. Parola, Mechanically stable and photocatalytically active TiO_2 /SiO_2 hybrid films on flexible organic substrates, J Mater Chem A. 2 (2014) 20096–20104.

[65] S. Pigeot-Rémy, F. Dufour, A. Herissan, V. Ruaux, F. Maugé, R. Hazime, C. Foronato, C. Guillard, C. Chaneac, O. Durupthy, C. Colbeau-Justin, S. Cassaignon, Bipyramidal anatase TiO2

nanoparticles, a highly efficient photocatalyst? Towards a better understanding of the reactivity, Appl. Catal. B Environ. 203 (2017) 324–334.

[66] Y. Dehmani, H. Lgaz, A.A. Alrashdi, T. Lamhasni, S. Abouarnadasse, I.-M. Chung, Phenol adsorption mechanism on the zinc oxide surface: Experimental, cluster DFT calculations, and molecular dynamics simulations, J. Mol. Liq. 324 (2021) 114993.

[67] J. Wang, Y. Xia, Y. Dong, R. Chen, L. Xiang, S. Komarneni, Defect-rich ZnO nanosheets of high surface area as an efficient visible-light photocatalyst, Appl. Catal. B Environ. 192 (2016) 8–16.

[68] J. Wang, Y. Xia, H. Zhao, G. Wang, L. Xiang, J. Xu, S. Komarneni, Oxygen defects-mediated Z-scheme charge separation in g-C3N4/ZnO photocatalysts for enhanced visible-light degradation of 4-chlorophenol and hydrogen evolution, Appl. Catal. B Environ. 206 (2017) 406–416.

Graphical Abstract